Analysis of hyperspectral fluorescence images for poultry skin tumor inspection

Seong G. Kong, Yud-Ren Chen, Intaek Kim, and Moon S. Kim

We present a hyperspectral fluorescence imaging system with a fuzzy inference scheme for detecting skin tumors on poultry carcasses. Hyperspectral images reveal spatial and spectral information useful for finding pathological lesions or contaminants on agricultural products. Skin tumors are not obvious because the visual signature appears as a shape distortion rather than a discoloration. Fluorescence imaging allows the visualization of poultry skin tumors more easily than reflectance. The hyperspectral image samples obtained for this poultry tumor inspection contain 65 spectral bands of fluorescence in the visible region of the spectrum at wavelengths ranging from 425 to 711 nm. The large amount of hyperspectral image data is compressed by use of a discrete wavelet transform in the spatial domain. Principal-component analysis provides an effective compressed representation of the spectral signal of each pixel in the spectral domain. A small number of significant features are extracted from two major spectral peaks of relative fluorescence intensity that have been identified as meaningful spectral bands for detecting tumors. A fuzzy inference scheme that uses a small number of fuzzy rules and Gaussian membership functions successfully detects skin tumors on poultry carcasses. Spatial-filtering techniques are used to significantly reduce false positives. © 2004 Optical Society of America

OCIS codes: 170.6510, 330.6180.

1. Introduction

Hyperspectral imaging combines the photonic technologies of conventional imaging and spectroscopy to produce images whose picture element (pixel) is associated with a spectral signature (spectrum). The spectral information provided by this pixel is valuable in the discrimination, detection, and classification of elements and structures within the image.[1] Each hyperspectral image pixel is typically composed of hundreds of contiguous narrow bands from the electromagnetic spectrum. The data produced by hyperspectral imaging sensors constitute a three-dimensional (3D) cube in two spatial dimensions and one spectral dimension. Spectral components to be measured often involve quantities such as reflectance and fluorescence ranging from the visible to short-wave infrared. This spectral imaging has the ability to exploit multiple regions of the electromagnetic spectrum to probe and analyze the composition of a material. The materials comprising various objects in a scene reflect, absorb, and emit electromagnetic radiation in amounts that vary with the wavelength. If the radiation arriving at the sensor is measured over a sufficiently broad spectral range, the resulting spectral signature can be used to uniquely characterize and identify any given material. Hyperspectral imaging systems have been utilized in a wide variety of scientific disciplines[2,3] that include airborne–satellite remote sensing of Earth resources, environmental monitoring, mapping of the Earth, management of water or agricultural resources, forestry, microscopic studies, agricultural product inspection, and the detection and classification of hidden targets in military applications.

One area of application that uses machine-vision systems is inspection and quality control in automated production processes.[4] Manufacturers in many industries depend on machine-vision inspection systems in order to produce high-quality products. Traditionally, the inspection processes are performed by trained human inspectors, and, typically, a small number of representative samples from a large production run are examined. The inspection and classification of agricultural products can be
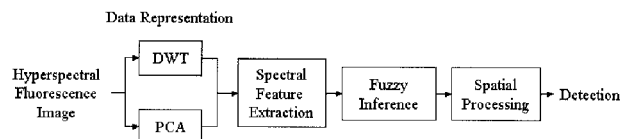
Fig. 1. Procedure of hyperspectral image analysis for poultry skin tumor inspection.

a highly repetitive and tedious task. Poultry carcasses with pathological problems must be identified and removed from food-processing lines to ensure wholesome products. Human inspectors are often required to examine 30–35 poultry samples per minute in the course of an 8-h day. Such working conditions can lead to repetitive motion injuries and attention and fatigue problems. Rapid, noninvasive machine-vision inspection methods for assessing hazardous conditions in food production would provide a substantial benefit in the quest to ensure the highest quality of inspection.

Hyperspectral imagery shows great potential for detection and classification of biomedical abnormalities because it provides both spatial and spectral features about the objects of interest in the image. A tumor is not as visually obvious as other pathological diseases such as septicemia, air sacculitis, and bruise because its spatial signature appears as a shape distortion rather than a discoloration. Poultry skin tumors are ulcerous lesions that are surrounded by a rim of thickened skin and dermis.[5] Tumorous carcasses may also have swollen or enlarged tissue caused by the uncontrolled growth of new tissue. Normal poultry skin often exhibits higher emissions compared with tumorous skin. Therefore conventional vision systems operating only in the visual spectrum may fail to meet every requirement of the high standards of a quality inspection. Detection of poultry skin tumors by use of hyper–multispectral imaging has been reported[6,7] to have the ability to differentiate wholesome and unwholesome agricultural products. Studies have also shown that the presence of defects is more easily detected by use of two or more bands of images from multispectral images.[8,9]

This paper presents an analysis of hyperspectral fluorescence images for detecting skin tumors on poultry carcasses. A number of compounds emit fluorescence in the visible region of the spectrum when excited with ultraviolet (UV) radiation.[10] It has been shown that fluorescence imaging reveals poultry skin tumors more easily than reflectance.[11] Figure 1 shows the proposed procedure of hyperspectral fluorescence image analysis for poultry skin tumor detection. An important function of hyperspectral image processing is to eliminate the redundancy in the spectral and spatial sample data while preserving the essential features needed for discrimination. Compression of the huge amount of hyperspectral data leads to significant reductions in computational complexity. The spatial content of hyperspectral images of poultry carcass samples are compressed by use of a discrete wavelet transform (DWT). Principal-component analysis (PCA) provides an efficient means for the compression of the spectral signatures without losing relevant information. Extraction of features indicative of spectral behaviors is preferable to a straightforward classification because it also leads to the reduction of computational complexity. This study utilizes the spectral bands that correspond to those spectral features that provide meaningful information for the detection of skin tumors. The hyperspectral imaging system described in this paper is used as a research tool to determine the several spectral bands that can be implemented in a multispectral imaging system for the on-line inspection of poultry carcasses. Features are obtained from the spectral peaks of relative fluorescence intensity of hyperspectral image samples. A fuzzy inference system with a small number of classification rules determines if a pixel belongs to normal skin or a tumor on the basis of these spectral features. Postprocessing with spatial-filtering techniques such as median and morphological filters removes false positives and refines the decision or classification.

2. Hyperspectral Fluorescence Imaging

A. Hyperspectral Fluorescence Imaging System

The Instrumentation and Sensing Laboratory (ISL) at Beltsville Agriculture Research Center has developed a laboratory-based line-by-line hyperspectral imaging system capable of reflectance and fluorescence imaging for uses in food safety and quality research.[11] It employs a pushbroom method in which a line of spatial information with a full spectral range per spatial pixel is captured sequentially to cover a volume of spatial and spectral data. The key components of the system are a CCD camera, a spectrograph, a sample transport mechanism, and appropriate lighting sources. Figure 2 shows a schematic diagram of the hardware components of the ISL hyperspectral imaging system.

The system is equipped with two independent illumination sources for reflectance and fluorescence measurements. For fluorescence measurement, two fluorescent lamp assemblies (Model XX-15A, Spectronics Corp., New York) provide a near-uniform UV-A (365-nm) excitation to the sample area. Short-pass filters (UG1, Schott Glass Co., Pennsylvania) placed in front of the lamp housings are used to prevent transmittance of radiations greater than approximately 400 nm and thus eliminate potential spectral contamination by incident light reflected from the sample at longer wavelengths. A precision positioning table transports sample materials through the line of field of view in a transverse direction while the stationary imaging system acquires data via line-by-line scans. The imaging system is a laboratory-based system designed for operation in a darkened room. Sample materials are placed on a tray painted with nonfluorescent, flat black paint to minimize background scattering.
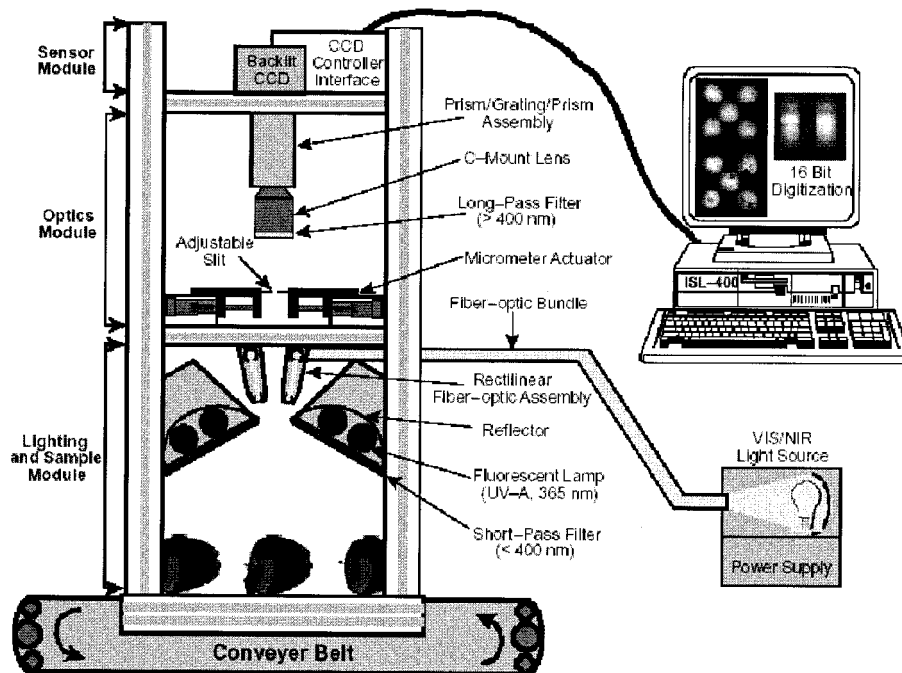
Fig. 2. Hardware components of the ISL hyperspectral imaging system.[11]   VIS, visible; NIR, near-infrared.

B. Acquisition of Hyperspectral Image Data

Hyperspectral sensors collect the spectral signatures of a number of contiguous spatial locations to form hyperspectral sensor imagery. A hyperspectral image can be represented as a 3D volume or cube of data; single-band images are stacked along a spectral axis. It contains spatial information measured at a sequence of individual wavelengths across a sufficiently broad spectral band. A hyperspectral image can be denoted by $\mathbf{I}(u, v, \lambda_i)$, where indices $u = 0, 1, \ldots, N - 1, v = 0, 1, \ldots, M - 1$ are spatial coordinates and $\lambda_i, i = 1, \ldots, L$, indicates spectral bands (channels).

The actual data format captured by the hyperspectral sensor is a two-dimensional (2D) array $U(p, q)$. By use of the fact that the qth column of U constitutes the image with the band λ_q, $U(p, q)$ can be easily converted into 3D image volume $\mathbf{I}(u, v, \lambda)$. For a fixed λ_k, $\mathbf{I}(u, v, \lambda_k)$ represents the kth-band image. If u and v are fixed, then $\mathbf{I}(u, v, \lambda)$ stands for spectrum or spectral information. Two images from adjacent bands (λ_j and λ_{j+1}) have a high degree of similarity, whereas images from distant bands can be less similar and may have independent information. Hyperspectral images are useful in the analysis of a scene as no single-band image has sufficient information to describe the information of the scene completely.

A total of 12 chicken carcasses were collected from a poultry processing plant (Allen Family Foods, Inc., Cordova, Maryland) in March and May 2002. The Food Safety and Inspection Service veterinarian at the plant identified the conditions of the chicken carcasses. They were put in plastic bags to minimize dehydration and then placed in a cooler with ice. The imaging measurements were conducted on the same day after the carcasses were transported to the ISL within 2 h. A typical hyperspectral image of a poultry sample consists of approximately $N = 460$, $M = 400$ pixels, each pixel with 1 mm $\times$ 1 mm spatial resolution. Each scan takes 0.5 s; thus it requires 200 s to complete a 3D hyperspectral image of a chicken sample. In this study, 65 spectral bands (L) from wavelength $\lambda_1 = 425.4$ nm to $\lambda_{65} = 710.7$ nm were used. Table 1 shows wavelength values of each spectral band. Figure 3 shows 12 spectral band images of a poultry carcass sample captured by use of the ISL hyperspectral fluorescence imaging system for $\lambda_5, \lambda_{10}, \ldots, \lambda_{60}$.

3. Hyperspectral Image Data Representation

A. Data Compression in the Spatial Domain

Hyperspectral data analysis requires efficient processing of the massive amount of data that result from the combination of spatial and spectral information acquired by the sensors. The high-dimensional data space generated by the hyperspectral sensors creates a new challenge for conventional spectral data analysis techniques. Dimensionality reduction can be achieved without significantly degrading detection performance or decreasing the separability among the different classes. A sample image of a poultry carcass has a spatial resolution of 460×400 pixels with 65 spectral bands. As each element is encoded by use of 16 bits, the resulting size of a sample poultry image will be approximately 24 megabytes ($= 460 \times 400$ pixels $\times$ 65 bands $\times$ 2 bytes). As a second example, one complete Airborne Visible–Infrared Imaging Spectrometer scene contains more than 140 megabytes ($= 224$ bands $\times 512 \times 614$ pix-

Band Number	Wavelength (nm)	Band Number	Wavelength (nm)	Band Number	Wavelength (nm)	Band Number	Wavelength (nm)
1	425.45	18	500.08	35	575.54	52	651.83
2	429.82	19	504.50	36	580.01	53	656.35
3	434.19	20	508.92	37	584.48	54	660.86
4	438.56	21	513.34	38	588.95	55	665.38
5	442.93	22	517.76	39	593.42	56	669.90
6	447.31	23	522.19	40	597.90	57	674.43
7	451.70	24	526.62	41	602.37	58	678.96
8	456.08	25	531.05	42	606.86	59	683.49
9	460.47	26	535.49	43	611.34	60	688.02
10	464.86	27	539.93	44	615.83	61	692.56
11	469.25	28	544.37	45	620.32	62	697.10
12	473.65	29	548.82	46	624.81	63	701.64
13	478.04	30	553.26	47	629.31	64	706.18
14	482.45	31	557.71	48	633.81	65	710.73
15	486.85	32	562.17	49	638.31		
16	491.26	33	566.62	50	642.81		
17	495.67	34	571.08	51	647.32		

els $\times$ 2 bytes). There is no doubt that the hyperspectral database will grow rapidly in size. The efficient distribution and use of this amount of information will be challenging.

The wavelet transform is a signal analysis tool that provides a systematic means for analyzing signals at various scales or resolutions. With DWTs,[12] signals are analyzed over a discrete set of scales. Typically, the discrete scales are dyadic (2, 4, 8, 16, . . .), and the transform can be implemented by use of a variety of fast algorithms and customized hardware. The most common implementation of the DWT is the multiresolutional dyadic filter tree implementation. The DWT can be described mathematically as a set of inner products between a finite-length sequence and a discretized wavelet basis. Each inner product re-

sults in a wavelet transform coefficient. Thus the DWT can be expressed as

$$W_f(j, k) = \sum_{n=0}^{N-1} f(n)\phi_{j,k}(n), \qquad (1)$$

where $W_f(j, k)$ is a DWT coefficient and $f(n)$ is a spectral signal with length N as a function of spectral band. The expression

$$\phi_{j,k}(n) = \frac{1}{\sqrt{2^j}} \phi\left(\frac{n - 2^j k}{2^j}\right) \qquad (2)$$

is the discretized wavelet basis, and 2^j and $2^j k$ are the discretized versions of the scale and translation parameters. In practice, the DWT can be implemented in a computationally efficient manner via the dyadic filter tree algorithm,[13] which represents the wavelet basis as a set of high-pass and low-pass filters in a filter bank. Level-1 discrete wavelet decomposition finds two signal components from the original signal by filtering with a low-pass filter and a high-pass filter. Following the filtering, the signal is decimated by a factor of 2. The outputs of the low-pass branch are called wavelet approximation coefficients A_j, and the outputs of the high-pass branch are called wavelet detail coefficients D_j of the original signal:

$$A_{j+1}(i) = \sum_{l=0}^{L-1} H(l)A_j(2i + l), \qquad (3)$$

$$D_{j+1}(i) = \sum_{l=0}^{L-1} G(l)A_j(2i + l). \qquad (4)$$

The functions G and H are the finite impulse responses of the high-pass and low-pass filters. A_0 is equal to the original signal $f(n)$.

The DWT can be effectively used to reduce a high volume of hyperspectral data.[14] For images, the wavelet decomposition is executed along the row- and
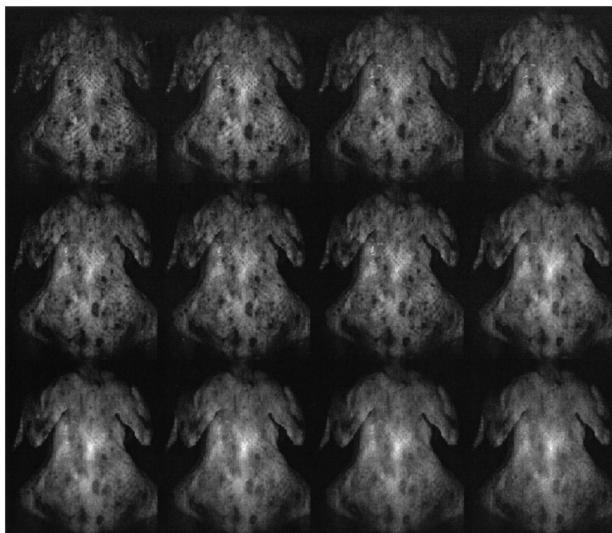

Fig. 3. Hyperspectral fluorescence images of a poultry carcass sample (bands 5, 10, through 60, for a total of 12 bands).
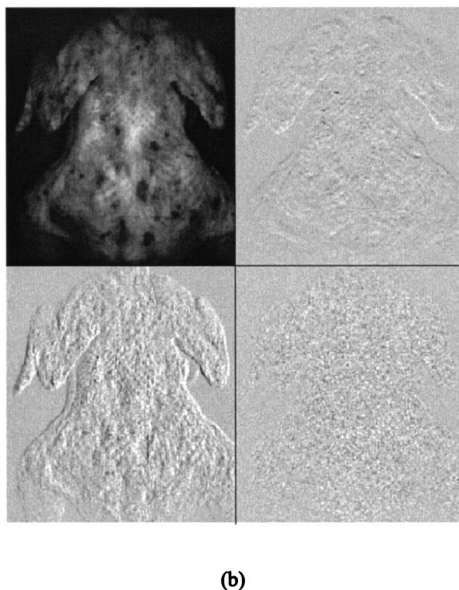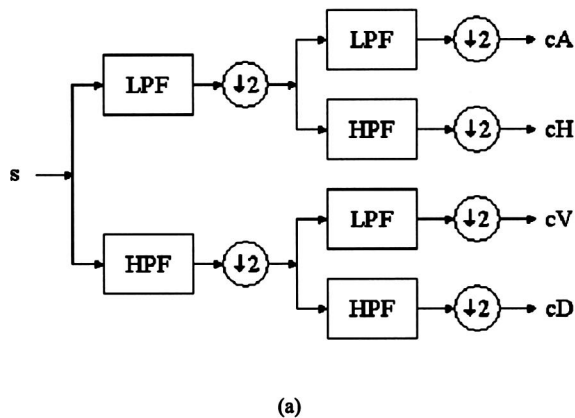
(a)

(b)

Fig. 4. Two-dimensional discrete wavelet decomposition. (a) Recursive filter tree implementation of the DWT. Filter banks for DWT. (b) Level-1 wavelet decomposition of a single-band image. Detail components are shown in reverse gray levels. LPF, low-pass filter; HPF, high-pass filter.

columnwise directions. The 2D wavelet decomposition transforms an image of $N \times M$ size to approximation (cA) and horizontal (cH), vertical (cV), and diagonal (cD) details of approximately $N/2 \times M/2$ size each. The approximation is the high-scale, low-frequency components of the signal. The details correspond to the low-scale, high-frequency components. Figure 4(a) shows a level-1 discrete wavelet decomposition procedure of a 2D image. Different choice of wavelets produces different sets of decomposed signals. Only the approximation component cA is used in the analysis to reduce the amount of data. The detail components cH, cV, and cD show relatively low energy content and therefore are not considered. Figure 4(b) shows the approximation and the detail components of a level-1 2D discrete wavelet decomposition of the band-5 poultry image sample. Detail components are shown in reverse gray levels. The

Daubechies wavelets of order 5 are used to decompose the hyperspectral images[15] into components. Visual characteristics are well preserved in the approximation component at a smaller image size.

B. Dimensionality Reduction in the Spectral Domain

PCA finds the best approximation that minimizes the sum of the squares of the errors introduced by the dimensionality reduction.[16] The goal of dimensionality reduction is to map data vectors $\mathbf{y}$ in an L-dimensional space $(y_1, \ldots, y_L)$ onto the feature vectors $\mathbf{a}$ in an M-dimensional space $(a_1, \ldots, a_M)$, with $M < L$. Let $\mathbf{e}_1, \ldots, \mathbf{e}_L$ be a set of eigenvectors of the covariance matrix of the n vectors $\mathbf{y}_1, \ldots, \mathbf{y}_n$ for training. Then a vector $\mathbf{y}$ can be represented as a linear combination of orthogonal eigenvectors as

$$\mathbf{y} = \sum_{i=1}^{L} a_i \mathbf{e}_i, \qquad (5)$$

where $a_i = \mathbf{e}_i^t \mathbf{y}$, $i = 1, \ldots, L$. One can achieve dimensionality reduction by retaining only a subset M of the basis vectors $\mathbf{e}_i$. Choosing eigenvectors corresponding to M largest eigenvalues minimizes the square error of approximation. The M coefficients a_i that represent the original data are referred to as principal components. The spectral dimension can be transformed into a vector space with M-dimensional space spanned by M principal components or factors. The first M factors account for most of the variance, with the first factor corresponding to the largest possible variance. The minimum error equals the sum of $L - M$ smallest eigenvalues. Each spectrum can be adequately represented by a few factors in factor space instead of the original spectral vectors. Figure 5 shows the eigenvectors and the energy content of the principal components obtained from the hyperspectral image data. The eigenvectors corresponding to the first three largest eigenvalues are shown in Fig. 5(a). Figure 5(b) reveals that most energy is concentrated on the first few components. The first three principal components retain almost all the energy of the spectral signature of hyperspectral image pixel.

Spectral characterization is crucial in hyperspectral image analysis. Figure 6 demonstrates that spectral signals of the hyperspectral images are represented with a small number of principal components. PCA(n) indicates spectral representation by use of the first n principal components. Owing to a relatively large number of normal pixels, the first PCA component closely represents the spectral characteristics of normal tissue. Five PCA components were enough to represent the spectral signals of both the normal and the tumor pixels.

4. Fuzzy Inference for Detecting Skin Tumors

A classifier is to distinguish skin tumors from normal tissue by use of the spatial and the spectral features of hyperspectral images.[17–19] Fuzzy inference schemes incorporate experts' domain knowledge into a mathematical model of decision making. In this
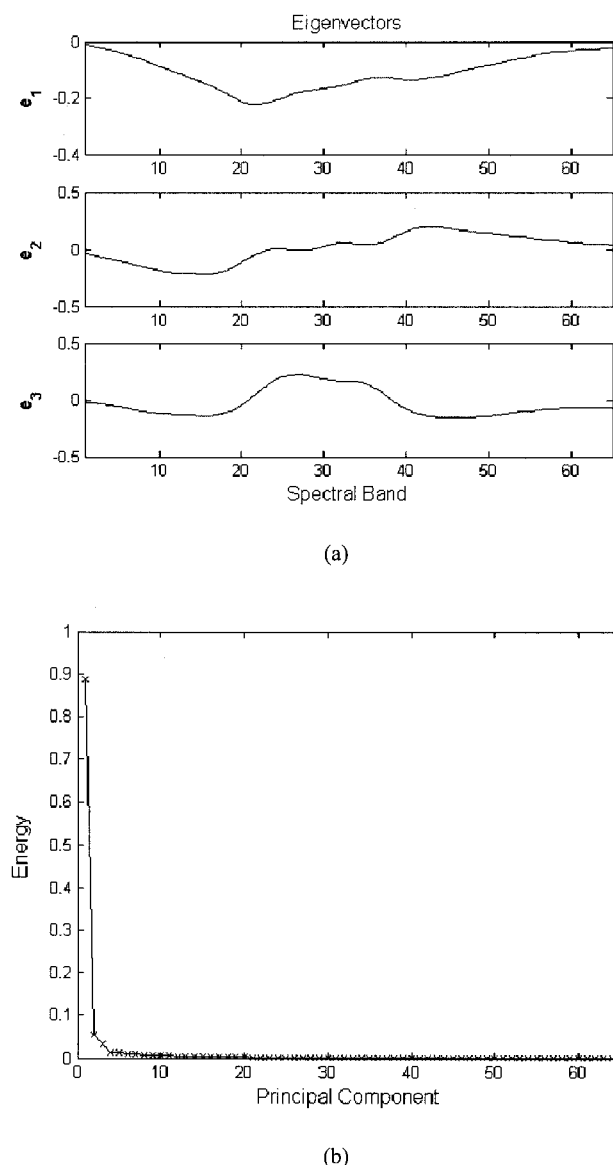
Fig. 5. PCA of spectral signatures. (a) The first three eigenvectors and (b) energy content of the principal components.

Fig. 6. Representation of spectral signals with a small number of principal components. (a) Normal tissue and (b) tumor.

paper a fuzzy classification system with a small number of fuzzy rules and features is proposed at a low classification system complexity as required in most practical vision-based inspection applications.

A. Feature Extraction

The spectral signature of fluorescence intensity reveals the characteristics of the normal tissues and tumors of poultry carcass skin. Figure 7 shows the relative fluorescence intensity of the pixel as a function of spectral bands for the three categories: normal, tumor, and background. A human skin tumor shows similar fluorescence responses in the blue-green regions of the spectrum when excited with 350-nm radiation.[20] Pixels obtained arbitrarily from the three tissue categories were used to obtain this graph. Normal tissues typically show higher
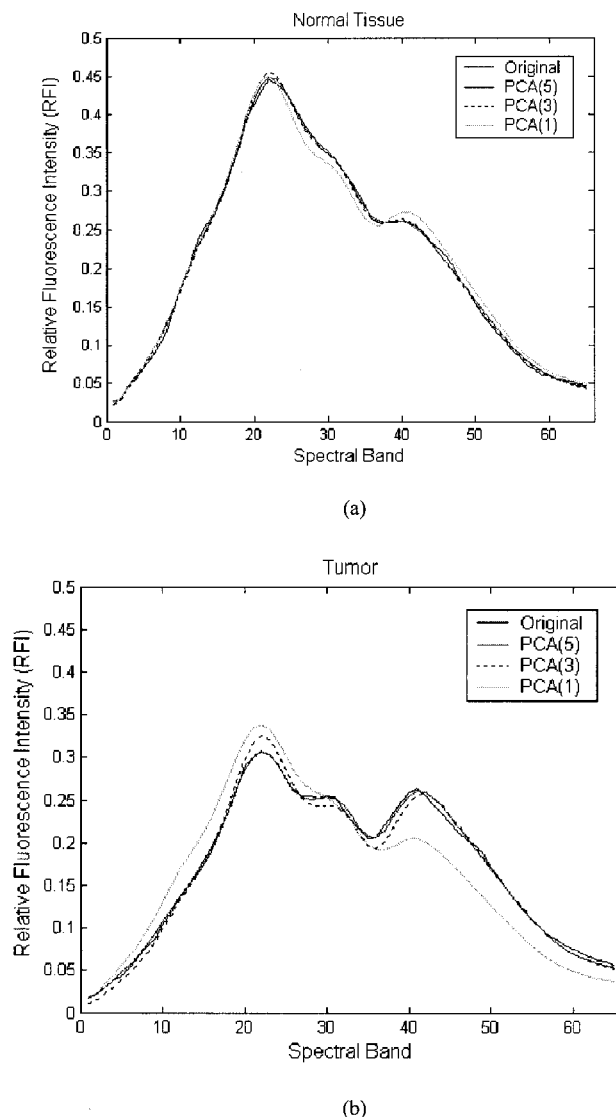
fluorescence emissions than tumors with relatively wide variations in fluorescence intensity. Normal tissues have a dominant peak response near band 20, whereas tumor tissues demonstrate multiple significant responses. Tumor pixels have lower fluorescence intensity on average but show strong responses near band 20 and at band 45, which make tumor pixels distinguishable from normal tissue. Background pixels show much lower fluorescence intensity with no spectral peaks owing to the tray painted with nonfluorescent, flat black paint.

Spectral characteristics of the pixels from the three categories can be utilized to define the features for tumor inspection. Features are computed from the level-1 approximation component of the discrete wavelet decomposition of hyperspectral image samples. The spectral signature used in this experiment is reconstructed from the first five principal components. Two features were obtained from the major
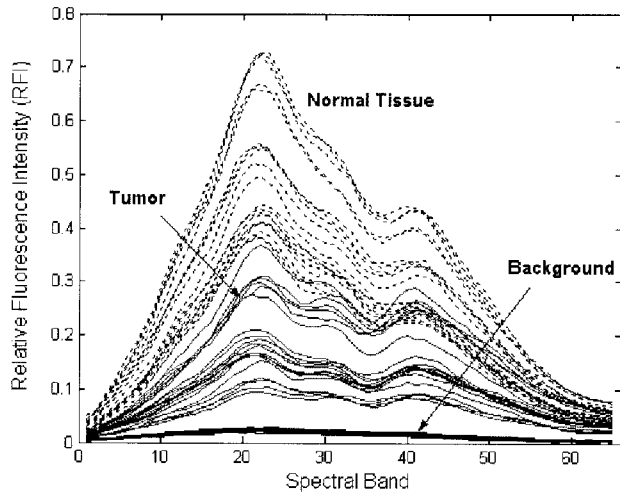
Fig. 7. Relative fluorescence intensity of normal tissue and tumor as a function of spectral bands.

Fig. 8. Scatter plot of the spectral features in the feature space.

spectral peaks of relative fluorescence intensity. The first major peak response is near band 20. The second peak response is identified as near band 45. Fluorescence emission from chicken tissues are broad in nature; thus a five-point running average over bands 44 to 48 was used to smooth the peak responses. The feature (x_1) defines the average fluorescence of the major peak response from bands 20 to 24. The second feature (x_2) measures the difference of the two peak responses. Equations (6) and (7) show the definitions of the two spectral features used in the classification:

$$x_1 = \frac{1}{5} \sum_{i=20}^{24} I(u, v, \lambda_i), \tag{6}$$

$$x_2 = \frac{\sum_{i=20}^{24} I(u, v, \lambda_i) - \sum_{i=44}^{48} I(u, v, \lambda_i)}{\sum_{i=20}^{24} I(u, v, \lambda_i)}. \tag{7}$$

Figure 8 shows a scatter plot of typical features from each category in the feature space x_1 and x_2. Selected features computed from the major peaks of the relative fluorescence intensity indicate that the feature space is well defined for our classification task. The features well represent the tumor and normal tissue classes with sufficient degree of separation.

B. Fuzzy Inference

Fuzzy logic is a superset of conventional logic that has been extended to handle the concept of partial truth. Truth values in fuzzy logic take on continuous values in the interval [0, 1], between completely true (1) and completely false (0). Conventional or Boolean logic uses the binary truth values of {0, 1}. Fuzzy logic is evolved from the notion of fuzzy sets in which an element can be a member of a fuzzy set to a degree between 0 and 1. Fuzzy rules can mathematically model the uncertainty of natural language.
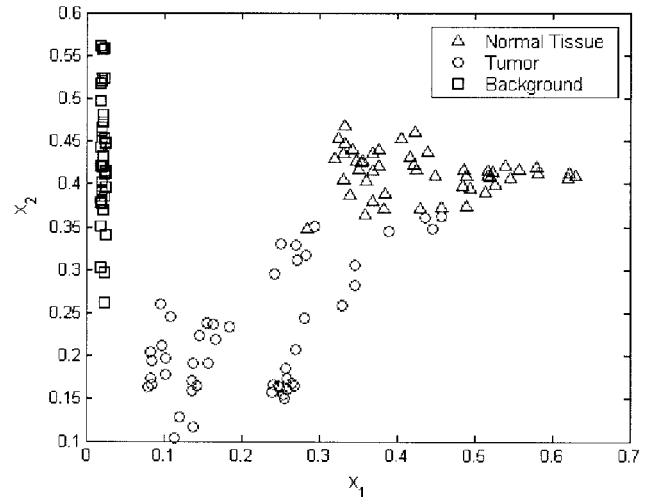
Fuzzy logic contains fuzzy rules usually represented in linguistic form.[21] A small number of fuzzy rules are introduced to classify tumors, normal tissue, and background in the hyperspectral images on the basis of the features defined in Eqs. (6) and (7). The two features x_1 and x_2 correspond to fuzzy variables with membership functions. The variable y indicates the output variable of the fuzzy system. Fuzzy decision rules for detecting poultry skin tumors can be articulated in the following linguistic forms:

Rule 1. If x_1 is medium (MED) and x_2 is small (SML), then y is tumor.
Rule 2. If x_1 is high (HGH) and x_2 is big (BIG), then y is normal.
Rule 3. If x_1 is low (LOW), then y is background (BG).

Three linguistic labels, LOW, MED, and HGH, are assigned to the fuzzy variable x_1. The variable x_2 has two labels, SML and BIG. All the labels are represented by the membership functions to represent the fuzziness nature of the measurement. Gaussian membership functions are adopted for their parametric forms. Equation (8) shows the Gaussian membership function of a fuzzy label A with the two parameters, the center c and the width w,

$$m_A(x) = \exp\left[-\frac{(x - c)^2}{2w^2} \right]. \tag{8}$$

Figure 9 shows the Gaussian membership functions for the two fuzzy variables x_1 and x_2. The membership functions are characterized by different values of center and width. In Fig. 9(a) the centers are 0, 0.2, and 1, and the corresponding widths are 0.05, 0.12, and 0.4. The membership functions in Fig. 9(b) have centers at 0 and 1 with corresponding widths of 0.12 and 0.3.

Fuzzy inference determines the degree (member-
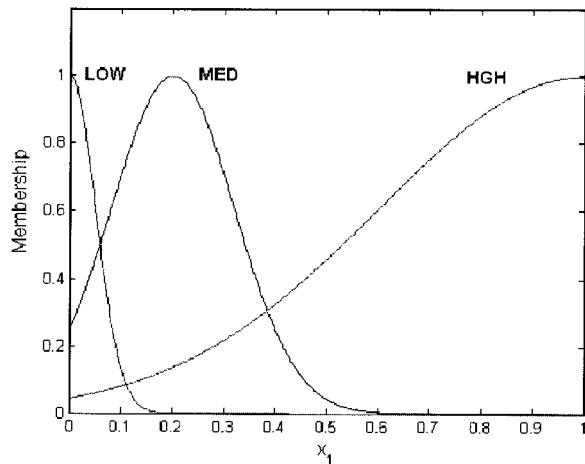
(a)
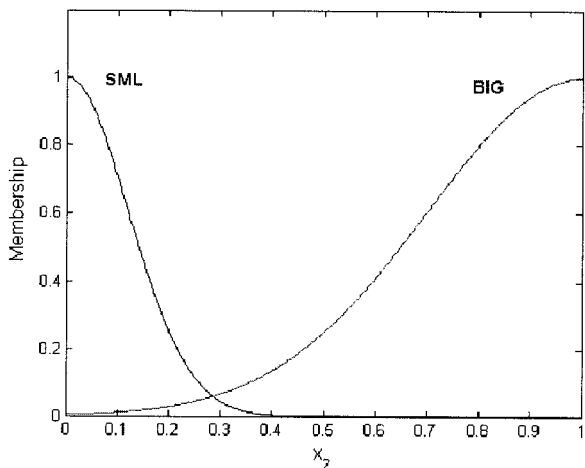
(b)

Fig. 9. Membership functions for the fuzzy variables x_1 and x_2. (a) Fuzzy variable x_1 (centers: 0, 0.2, 1; widths: 0.05, 0.12, 0.4) and (b) fuzzy variable x_2 (centers: 0, 1; widths: 0.12, 0.3).

ship value) to which a pixel belongs to a class. Fuzzy inference takes the conjunction operation of the fuzzy variables in each rule and aggregates partial output of all the fuzzy rules. The popular max–min fuzzy inference scheme adopts minimum (min) conjunction and maximum (max) aggregation. The minimum conjunction operation calculates the degree of firing as the minimum of corresponding membership values of the fuzzy variables:

$$m_{\text{TUMOR}}(y) = \min[m_{\text{MED}}(x_1), m_{\text{SML}}(x_2)], \quad (9)$$

$$m_{\text{NORMAL}}(y) = \min[m_{\text{HGH}}(x_1), m_{\text{BIG}}(x_2)], \quad (10)$$

$$m_{\text{BG}}(y) = m_{\text{LOW}}(x_1). \quad (11)$$

Rule aggregation procedure integrates partial outputs of all the fuzzy rules to produce a combined output. The max rule aggregation procedure finds the fuzzy decision as the maximum of the entire fuzzy
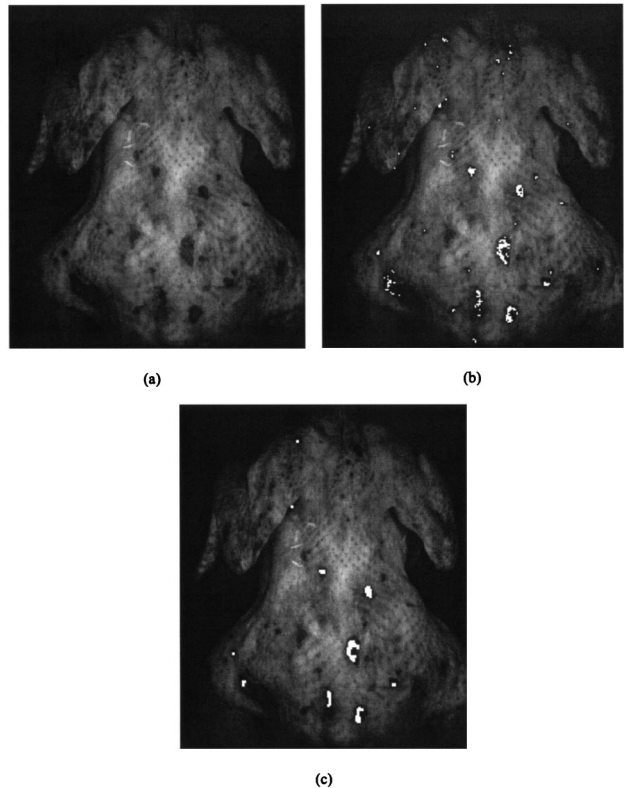

Fig. 10. Detection of tumors with the fuzzy classifier for the training sample of band 20 (λ_{20}). (a) Original image, (b) fuzzy inference system output, and (c) fuzzy inference system output with morphological filtering.

rule outputs as in Eq. (12), as the degree to which the fuzzy system output y belongs to one of the three categories:

$$m^*(y) = \max\{m_{\text{NORMAL}}(y), m_{\text{TUMOR}}(y), m_{\text{BG}}(y)\}. \quad (12)$$

The fuzzy inference output indicates the degree to which a pixel belongs to one of the three categories. Defuzzification finds the crisp (not fuzzy) decision output. The binary decision output that a pixel $I(u, v)$ is assigned to the tumor class can be represented by

$$D\{I(u, v)\} = \begin{cases} 1 & \text{if } m^*(y) = m_{\text{TUMOR}}(y) \\ 0 & \text{otherwise} \end{cases}. \quad (13)$$

Additive fuzzy systems use additive rule aggregation instead of the max operation. Often defuzzified output can be found as the centroid of the combined fuzzy rule outputs. The centroid fuzzy output y^* is computed as in Eq. (14), where y_1 denotes the class centroid for the normal class, y_2 for the tumor class, and y_3 for the background class:

$$y^* = \frac{y_1 m_{\text{NORMAL}}(y) + y_2 m_{\text{TUMOR}}(y) + y_3 m_{\text{BG}}(y)}{m_{\text{NORMAL}}(y) + m_{\text{TUMOR}}(y) + m_{\text{BG}}(y)}. \quad (14)$$
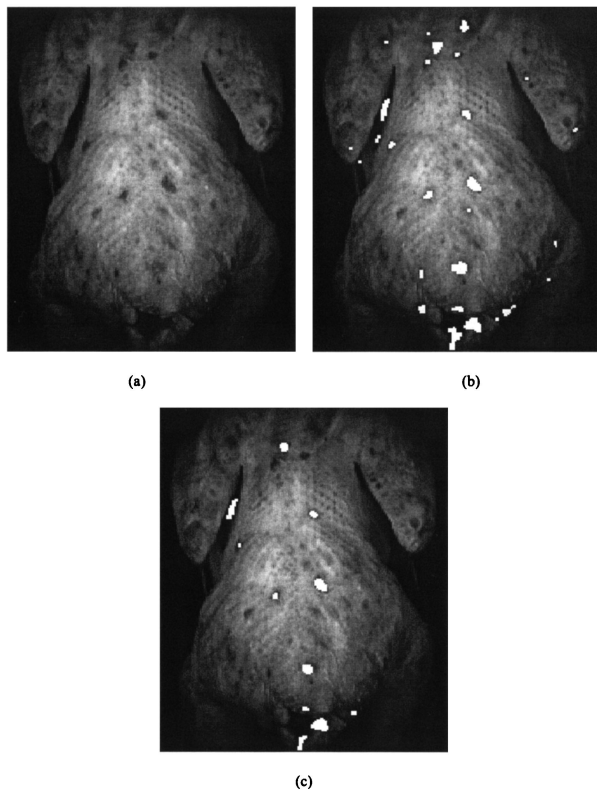
Fig. 11. Detection of tumors with the fuzzy inference system for testing sample of band 20 (λ_{20}). (a) Original image, (b) fuzzy system output, and (c) fuzzy system output with median filtering.

Then the decision by the additive fuzzy system becomes

$$D\{I(u, v)\} = \begin{cases} 1 & \text{if } y^* \in J(y_2) \\ 0 & \text{otherwise} \end{cases}, \qquad (15)$$

where $J(y_2)$ denotes the interval in the output space y that contains the centroid y_2 corresponding to the tumor category.

Among the twelve chicken samples, one chicken sample is used for training of the fuzzy system parameters, and eleven samples are used for testing. Figure 10 shows a poultry skin tumor detection result for the image used for training by the fuzzy inference system. Figure 10(a) shows the original image of band 20, Fig. 10(b) indicates the binary detection result $D\{I(u, v)\}$ by the fuzzy decision rules, and the postprocessing result that uses morphology filters is shown in Fig. 10(c). White dots superimposed on the image show the pixels of skin tumors classified by the fuzzy rules. Figure 11 shows the original image and classification result of a poultry sample not used in training. Median filtering of either 3×3 or 5×5 size applied to fuzzy classification output significantly reduces false positive alarms. Heuristics such as the knowledge that tumors often have oval or circular shapes or that tumors are likely bigger than a certain size can be used to further eliminate spurious tumor regions.

Table 2 summarizes the results of poultry skin tumor inspection that uses the fuzzy inference system with and without median filtering in the spatial domain. In both cases the fuzzy inference system achieved a detection rate of 82%. It is observed that isolated tumors are easily detected as long as they are big enough, but detection failure is likely to occur when tumors are located closely together. Missed tumors are attributed to a multiple of small, early-stage tumor spots. Spatial filtering such as morphological and median filtering significantly reduced the occurrence of false positive classifications.

5. Conclusion

The hyperspectral fluorescence imaging system developed by the Instrument and Sensing Laboratory, together with a fuzzy inference scheme, finds an effective machine-vision approach for the detection of skin tumors on poultry carcasses. Skin tumors are not as visually obvious as other pathological diseases because the signature usually appears as a shape distortion rather than a discoloration. This fact makes it difficult to conduct regular pattern-recognition tasks based on the reflectance images. The hyperspectral imaging system captures the

Table 2. Classification Performance

Image Number	Number of Tumors	Fuzzy Classifier			Fuzzy Classifier with Spatial Filtering		
		Number found	False positive	Number missed	Number found	False positive	Number missed
1	8	8	3	0	8	2	0
2	2	2	2	0	2	0	0
3	0	0	0	0	0	0	0
4	3	3	2	0	3	1	0
5	2	2	2	0	2	2	0
6	2	1	1	1	1	1	1
7	2	2	1	0	2	0	0
8	0	0	0	0	0	0	0
9	4	3	1	1	3	0	1
10	7	3	2	4	3	1	4
11	3	3	2	0	3	1	0
Total	33	27 (82%)	16	6 (18%)	27(82%)	8	6 (18%)

fluorescence image data from poultry samples. Features obtained from the fluorescence images demonstrate superior contrast and therefore provide a better discrimination capability for poultry skin tumor detection. A large amount of hyperspectral data is compressed in the spatial domain by use of discrete wavelet transforms. The principal-component analysis gives an effective representation of spectral signatures in terms of a few principal components for the purpose of data compression in the spectral domain. A fuzzy inference system with a small number of decision rules was developed for detecting poultry skin tumors. The level-1 approximation of the DWT was used to extract the features for skin tumor detection. Two features are obtained from the two dominant spectral peaks of the relative fluorescence intensity distribution as a function of spectral bands. The first feature measures the average intensity of the dominant peak, which consists of spectral bands 20 to 24. The second feature is created from the difference of the dominant peak of the first feature and the spectral peak observed from bands 44 to 48. The fuzzy inference system utilizes these two features as inputs for inference. A small number of fuzzy rules using the max–min fuzzy inference scheme successfully detect poultry skin tumors. The use of spatial filtering with morphological and median filters decreases the number of false positive classifications.

References

1. D. A. Landgrebe, "Hyperspectral image data analysis as a high dimensional signal processing problem," IEEE Signal Process. Mag. **19,** 17–28 (2002).

2. H. Holden and E. LeDrew, "Spectral discrimination of healthy and non-healthy corals based on cluster analysis, principal components analysis, and derivative spectroscopy," Remote Sens. Environ. **65,** 217–224 (1998).

3. D. W. Lamb and R. B. Brown, "Remote-sensing and mapping of weeds in crops," J. Agric. Eng. Res. **78,** 117–125 (2001).

4. A. Rosenfeld, "Computer vision: basic principles," Proc. IEEE **76,** 863–868 (1988).

5. B. W. Calnek, H. J. Barnes, C. W. Beard, W. M. Reid, and H. W. Yoder, *Diseases of Poultry* (Iowa State University, Ames, Iowa, 1991), Chap. 16, pp. 386–484.

6. K. Chao, Y. R. Chen, W. R. Hruschka, and F. B. Gwozdz, "On-line inspection of poultry carcasses by a dual-camera system," J. Food Eng. **51,** 185–192 (2002).

7. Y. R. Chen, B. Park, R. W. Huffman, and M. Nguyen, "Classification of on-line poultry carcasses with backpropagation neural networks," J. Food Process. Eng. **21,** 33–48 (1998).

8. B. Park, Y. R. Chen, M. Nguyen, and H. Hwang, "Characterizing multispectral images of tumorous, bruised, skin-torn, and wholesome poultry carcasses," Trans. ASAE **39,** 1933–1941 (1996).

9. Z. Wen and Y. Tao, "Fuzzy-based determination of model and parameters of dual-wavelength vision system for on-line apple sorting," Opt. Eng. **37,** 293–299 (1998).

10. E. W. Chappelle, J. E. McMurtrey, and M. S. Kim, "Identification of the pigment responsible for the blue fluorescence band in laser induced fluorescence spectra of green plants, and potential use of this band in remotely estimating rates of photosynthesis," Remote Sens. Environ. **36,** 213–218 (1991).

11. M. S. Kim, Y. R. Chen, and P. M. Mehl, "Hyperspectral reflectance and fluorescence imaging system for food quality and safety," Trans. ASAE **44,** 721–729 (2001).

12. S. G. Mallat, "A theory for multiresolution signal decomposition: the wavelet representation," IEEE Trans. Pattern Anal. Mach. Intell. **11,** 674–693 (1989).

13. S. Burrus, R. Gopinath, and H. Guo, *Introduction to Wavelets and Wavelet Transforms: A Primer*, 1st ed. (Prentice-Hall, Englewood Cliffs, N.J., 1998).

14. P. Luigi-Dragotti, G. Poggi, and A. R. P. Ragozini, "Compression of multispectral images by three-dimensional SPIHT algorithm," IEEE Trans. Geosci. Remote Sens. **38,** 416–428 (2000).

15. I. Daubechies, *Ten Lectures on Wavelets*, Vol. 61 of Conference Board of the Mathematical Sciences–National Science Foundation Regional Conference Series in Applied Mathematics, (Society for Industrial and Applied Mathematics, Philadelphia, Pa., 1992).

16. C. M. Bishop, *Neural Networks for Pattern Recognition* (Oxford U. Press, New York, N.Y., 1995).

17. S. M. Schweizer and J. M. F. Moura, "Efficient detection in hyperspectral imagery," IEEE Trans. Image Process. **10,** 584–597 (2001).

18. D. S. Jayas, J. Paliwal, and N. S. Visen, "Multi-layer neural network for image analysis of agricultural products," J. Agric. Eng. Res. **77,** 119–128 (2000).

19. B. Park, Y. R. Chen, and M. Nguyen, "Multi-spectral image analysis using neural network algorithm for inspection of poultry carcasses," J. Agric. Eng. Res. **69,** 351–363 (1998).

20. L. Brancaleon, A. J. Durkin, J. H. Tu, G. Menaker, J. D. Fallon, and N. Kollias, "*In vivo* fluorescence spectroscopy of nonmelanoma skin cancer," Photochem. Photobiol. **73,** 178–183 (2001).

21. S. G. Kong and B. Kosko, "Adaptive fuzzy system for backing up a truck-and-trailer," IEEE Trans. Neural Netw. **3,** 211–223 (1992).